Philosophical Magazine

ISSN: 1478-6435 (Print) 1478-6443 (Online) Journal homepage: www.tandfonline.com/journals/tphm20

Depth defect analysis of BaO thin films doped with Cd via positron annihilation techniques

Mohamed El Amine Dahamni, Nassima Hamzaoui, Mostefa Ghamnia, Murat Yavuz Yener, Ayse Yumak, Cumali Tav & Ugur Yahsi

To cite this article: Mohamed El Amine Dahamni, Nassima Hamzaoui, Mostefa Ghamnia, Murat Yavuz Yener, Ayse Yumak, Cumali Tav & Ugur Yahsi (11 Jan 2026): Depth defect analysis of BaO thin films doped with Cd via positron annihilation techniques, Philosophical Magazine, DOI: 10.1080/14786435.2025.2601438

To link to this article: https://doi.org/10.1080/14786435.2025.2601438

Published online: 11 Jan 2026.

PHILOSOPHICAL MAGAZINE
https://doi.org/10.1080/14786435.2025.2601438

Taylor & Francis
Taylor & Francis Group

Depth defect analysis of BaO thin films doped with Cd via positron annihilation techniques

Mohamed El Amine Dahamni[a], Nassima Hamzaoui[a], Mostefa Ghamnia[a], Murat Yavuz Yener[b], Ayse Yumak[c], Cumali Tav[c] and Ugur Yahsi[c]

[a]LSMC Laboratory, Oran 1 Ahmed Ben Bella University, Es-sénia, Algeria; [b]BETAM, Fatih Sultan Mehmet Vakıf University Topkapı Campus, Istanbul, Turkiye; [c]Department of Physics, Faculty of Science, Marmara University, Istanbul, Turkiye

ABSTRACT

Thin films of pure and cadmium-doped barium oxide (BaO) with 2, 4, and 6 wt% Cd were made using the spin-coating method and placed on glass at 450°C. Atomic force microscopy (AFM) revealed coarse, textured surfaces with BaO crystallites ranging from 1.4 to 150 nm in size, depending on the Cd concentration. Optical properties were investigated using UV–visible spectroscopy, revealing high transparency and direct bandgap energies between 3.467 and 3.728 eV. Defects were studied using Doppler broadening spectroscopy (DBS), which showed that there were different types of defects linked to oxygen and barium. A correlation was observed between the S parameter of DBS, crystallite size, and optical bandgap. Additionally, positron annihilation lifetime spectroscopy (PALS) was used to study vacancy-type defects and verify the positron lifetimes connected to the S parameter. The results demonstrate that Cd doping significantly influences the microstructure, defect landscape, and optoelectronic properties of BaO thin films.

ARTICLE HISTORY
Received 16 May 2025
Accepted 4 December 2025

KEYWORDS
BaO; vacancy defects; oxygen and barium defects; Doppler broadening spectroscopy; positron annihilation lifetime spectroscopy

1. Introduction

Barium oxide (BaO) in nanometric films has attracted widespread attention because of its interesting structural, optical, and electrical properties in many fields, such as electron field emission, gas sensors, solar energy conversion, catalysis, electronic devices, and optoelectronic device applications [1–5]. At low dimensionality, BaO in thin films behaves like transparent conducting oxide (TCO) materials, which have semiconductor properties with a direct bandgap of 4.4 eV [6]. Doping BaO further improves its physical properties and is an effective approach for tuning their electronic, magnetic, structural and optical properties for various desired applications.

In this work, we chose to dope BaO films with cadmium because it is an element that has the same valence as Ba, and the ratio of their atomic radii is significantly greater than one, allowing an easy insertion of cadmium into the barium site in the BaO lattice.

CONTACT Ugur Yahsi uyahsi@marmara.edu.tr Department of Physics, Faculty of Science, Marmara University, Goztepe Campus, 34722 Kadikoy, Istanbul, Türkiye; Mostefa Ghamnia mgghamnia@yahoo.fr LSMC Laboratory, Oran 1 Ahmed Ben Bella University, Es-sénia, 31100, Algeria

According to our research, there are almost no studies that have studied the Cd-doping of BaO films.

Many preparation methods, such as spin coating, spray pyrolysis, and quick precipitation [7–10], have been developed to synthesise BaO thin films. Among these methods, the spin-coating technique has gained much popularity because of its facile synthesis method, its inexpensive approach for good yield, and especially its ability to obtain high-quality films. We used this synthesis route to prepare pure and Cd-doped BaO films from barium acetate dihydrate ($\underline{C_4H_{10}BaO}$, $2H_2O$) as the inorganic precursor. We also investigated the influence of cadmium (Cd) doping on the crystalline quality of BaO nanofilms. All the deposits were made on glass substrates heated to 450°C. Characterisation of the morphology and optical properties of the prepared pure and Cd-doped BaO nanofilms was performed via atomic force microscopy (AFM) and UV–visible spectroscopy. Defects in BaO films were analysed via Doppler broadening spectroscopy (DBS) and positron annihilation lifetime spectroscopy (PALS).

The main focus of this study is to utilise the DBS approach to retrieve the vacancy defect indicated by *S* and its counterpart indicated by *W* as a measure of chemical defects. On the other hand, another useful nondestructive positron technique is positron annihilation lifetime spectroscopy (PALS), which is a very advantageous, adaptable, and potent methodology with widespread use in diverse scientific and industrial domains. It provides significant information about the atomic and molecular structure of materials and any imperfections or vacancy defects inside them. This makes it useful for both research purposes and technological applications.

2. Experimental procedure

2.1. Chemical preparation of samples

Pure and cadmium-doped barium oxide thin films were obtained by depositing the prepared aqueous solution onto heated glass substrates via the spin-coating technique. The primary solution permitting the extraction of pure barium oxide was prepared with 0.2 M/l barium acetate dihydrate ($\underline{C_4H_{10}BaO}$, $2H_2O$) in 100 ml of deionised water. A secondary solution prepared from cadmium acetate dehydrate ($(CH_3COO)_2Cd$, $2H_2O$) at different concentrations was added to the primary solution to obtain Cd-BaO-doped films at Cd/Ba ratios of 2%, 4%, and 6%. These solutions were deposited onto heated glass substrates maintained at 450°C.

2.2. Characterisation techniques

The prepared samples were characterised by the use of different experimental techniques. The morphology and the optical properties were optained from atomic force microscope (AFM) and UV-visible spectroscopy respectively.. Dimension Edge AFM from Bruker is very sensitive to the surface morphology, UV–visible spectrometer using a Specord 50 Plus, Analytik Jena, Jena, Germany, gives a good results for optical analysis.

The defects in pure and Cd-doped BaO were characterised by Doppler broadening spectroscopy (DBS) and positron annihilation lifetime spectroscopy (PALS) for defects.

The DBS approach relies on Doppler broadening of the annihilation gamma. When a positron comes into contact with an electron in a material, the momentum of the combined positron–electron system is transmitted to the 511 keV annihilation gamma line, causing it to broaden due to the Doppler shift [11]. The Doppler broadening spectrum can be divided into five distinct parts, focusing on the centre and wing parts. The parameters *S* (sharpness) and *W* (wing) are defined as the ratios of the centre and wing parts, respectively, to the overall area of the peak [11]. The *S* and *W* parameters vary due to positron annihilation in the vacancy defect in the material, with low and high momenta of the valence and core electrons, respectively, leading to an increase or decrease. The *S* and *W* parameters are not fixed values; however, in this study, we select the *S* parameter to set the middle part of the annihilation gamma of the Si single-crystal to 0.5 and the *W* parameter to set the corresponding wing parts to 0.050 [11–13].

In addition to the *S* and *W* parameters, an additional parameter, *P*, as a measure of porosity, is derived from the spectrum. *P* represents the ratio of the combined area of the valley region (which lies between the Compton edge and the annihilation line) to the total area of the annihilation peak at 511 keV [14]. The first phenomenon is caused by the annihilation of ortho-positronium (o-Ps) through the emission of three gamma rays (3γ), whereas the second phenomenon is caused by the annihilation of para-positronium (p-Ps) through the emission of two gamma rays (2γ). The presence of the pore structure in the material influences the parameter *P* [12–14]. The DBS setup comprises a Canberra GC2519 HPGe detector, an ORTEC572A amplifier, and an ORTEC ASPEC-927 MCA [12,13].

PALS is a noninvasive technique for studying atomic-level defects and structural properties. The primary goal of the PALS system is to accurately measure the time interval between the emission of the starting signal at 1274 keV and the annihilation signal at 511 keV. To accomplish this, a fast-fast coincidence system is employed [11].

The positron source utilised in the experiment was made by depositing and evaporating approximately 30 μCi of a 22NaCl aqueous solution onto a 7 μm Kapton film. This source was then sandwiched between two samples: one consisting of just substrate glass and the other consisting of a BaO film along with the substrate. Source contribution has been considered in the analysis of the spectrum.

The PALS setup consists of two ultrafast gamma scintillator detectors: each consists of a BC422 plastic scintillator photocoupled with a Hamamatsu R2059 photomultiplier tube with an Ortec 265A base. We employed a constant fractional differential discriminator for the energy window of gamma selection and timing (Ortec CFDD 583B). The time difference between two gammas is converted by a time-to-amplitude converter (TAC 566, Ortec) and then fed into a multichannel analyzer (ASPEC 927 MCA, Ortec). The spectroscopic data obtained from the MCA comprises at least one million counts to statistically obtain the confidence parameters of lifetimes and intensities.

A lifetime spectrum typically consists of three components, each characterised by its own corresponding states. The shortest positron lifetime (τ_1) typically represents positron annihilation at defect-free sites, which serves as a characteristic parameter of the structure. The next-shortest lifetime (τ_2) is associated with positrons confined at mono- or divacancy defect sites or direct annihilation. The longest lifetime (τ_3) is related to the annihilation of o-Ps atoms formed inside sufficient voids or the positioning

of positrons at vacant spaces. Using LT9.3 software [15], we obtained the PALS parameters described above, which were used to convolve the spectra.

3. Results and discussion

3.1. Atomic force microscopy (AFM) analysis

Atomic force microscopy (AFM) was used to study the morphology of diverse surfaces of BaO samples. AFM analysis is ideal for quantitatively measuring the nanometer-scale surface roughness and for visualising the nanotextured and relieved surfaces of a film. Pure and Cd-doped BaO films were investigated by AFM in contact mode to study the morphology of their surfaces and determine the effect of Cd doping on improving surface morphology. AFM images of the samples were acquired under ambient conditions via Dimension Edge AFM (Bruker Model) and analysed via WsXM software [16]. The AFM images are shown in Figure 1. From the AFM images (a, d, g, j), we observe a porous, inhomogeneous, and discontinuous surface of the pure and Cd-BaO films. The surface is formed by crystallites of different sizes separated by voids (dark areas) corresponding to the glass substrate. As shown by the profiles taken on a horizontal line in each image, the crystallite size decreases drastically from 150 nm for the pure BaO to 1.4 nm for the 6% Cd-doped BaO films. This observation of the crystallites agrees well with the roughness analysis shown in the plots (c, f, i, m). From the profile and roughness plots, it seems that Cd doping affects the decrease in the crystallite size and improves the surface morphology.

3.2. Optical properties

The optical properties were determined by measuring the transmittance (T) and absorbance (α) of the BaO films via UV–visible spectroscopy with a double-beam spectrophotometer. T and α spectra were recorded in the 275–450 nm range, as shown in Figure 2(a). The transmittance clearly indicates that the pure and Cd-doped BaO films are transparent, but the transmittance yield decreases from 70% for the pure BaO films to 50% for the Cd-doped BaO. This decrease due to doping effects has already been reported in previous works [17,18]. The transmittance yield is affected by doping, which reduces the size of the surface grains and improves the surface morphology.

We can plot Tauc's equation [19], which is given by Equation (1), by combining the transmittance and absorption data. This gives us the relationship between the photon's incident energy and the material films' absorption coefficient as

$$(\alpha h\nu)^2 = A(h\nu - E_g) \tag{1}$$

where α is the absorption yield, $h\nu$ is the photon energy, A is a constant, and E_g is the band gap energy. The plot of $(\alpha h\nu)^2$ versus $(h\nu)$ is shown in Figure 2(b).

According to Equation (1), the extrapolation of the linear part of the curve between $(\alpha h\nu)^2$ and the photon energy $(h\nu)$ until the intersection with the $h\nu$ axis gives the E_g band gap values. The determined E_g values of the pure and Cd-doped films are presented in Table 1.

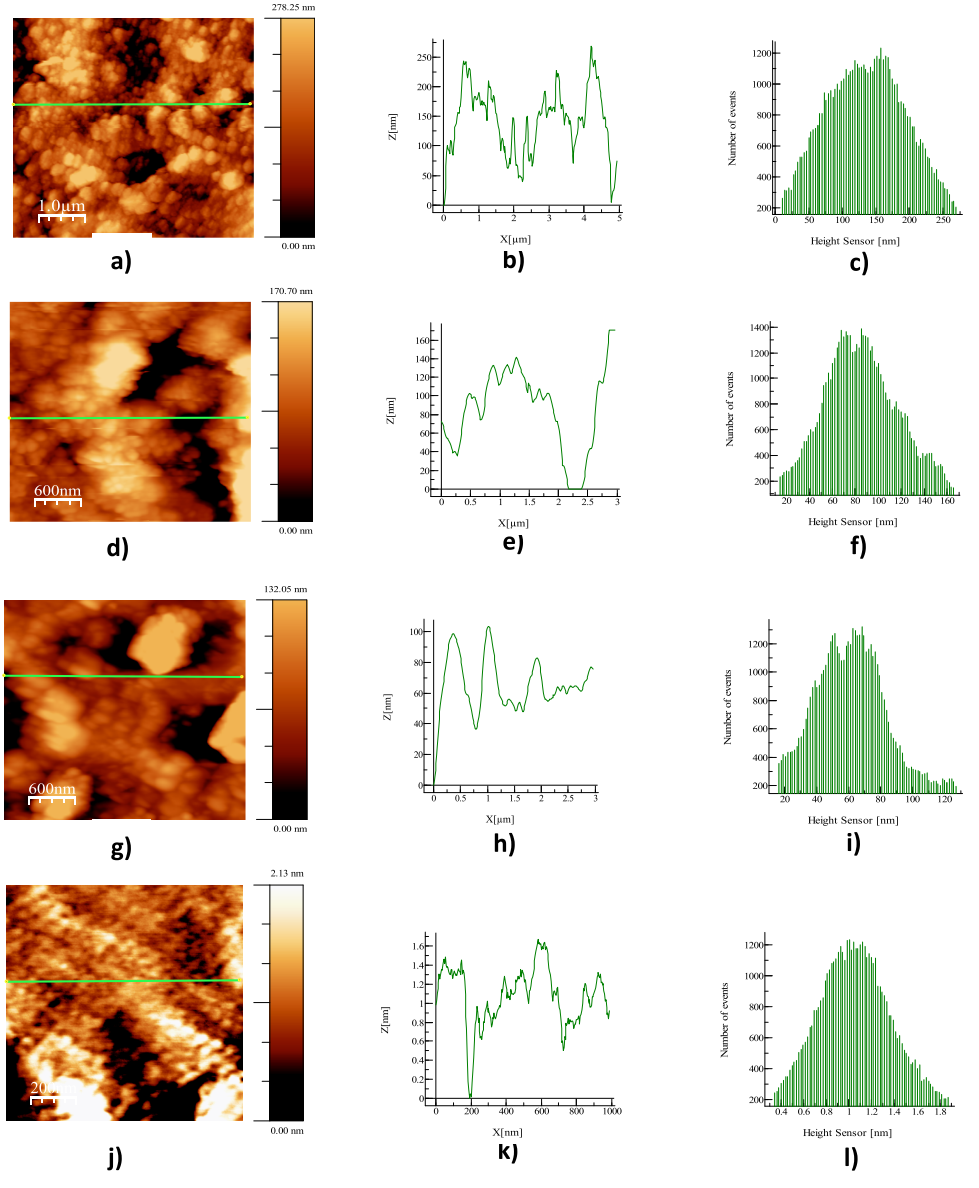

Figure 1. AFM images of pure and Cd-doped BaO films: (a, d, g, j): surface morphology of pure and 2, 4, and 6% Cd-doped BaO films. (b, e, h, k): surface profiles plotted along the horizontal lines shown on the corresponding AFM images, (c, f, i, l) roughness profiles from the AFM images.

Table 1. Bandgap energy of the samples graphically determined from the plot of Tauc's equation and some values reported in the literature.

Sample	E_g (eV)	E_g (eV) in literature
Pure BaO	3.467	4.65 [20]
2% Cd-doped BaO	3.617	2.4-2.6 [2]
4% Cd-doped BaO	3.664	3.70 [21]
6% Cd-doped BaO	3.728	

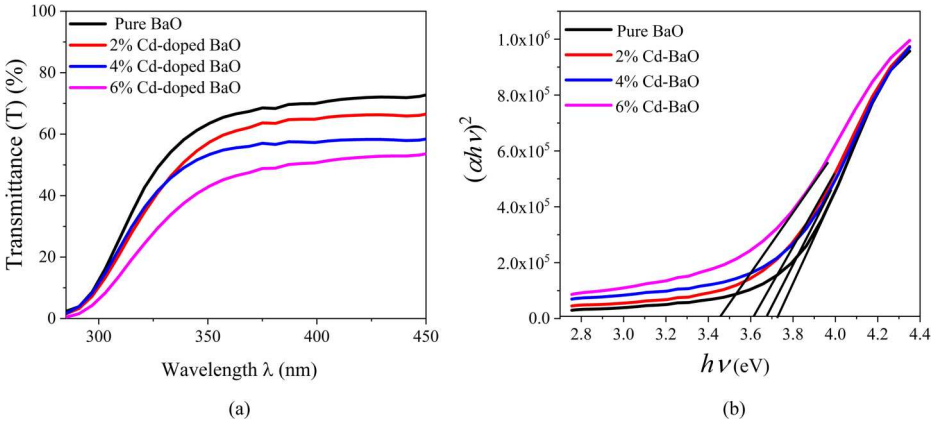

Figure 2. (a) Transmittance spectra of pure and Cd-doped BaO and (b) Tauc plot $(ahv)^2$ vs hv for energy gap determination.

From Table 1, the band gap energy values obtained in our work are in the range of 3.467 – 3.728 eV, which are in fair agreement with those reported in the literature [2,20,21]. Furthermore, the energy gap of Cd-doped BaO increases with increasing Cd doping.

3.4. The Doppler broadening spectroscopy (DBS) results

The DBS setup was used to obtain the energy spectrum of the annihilation gammas. Each spectrum comprises one million counts. The SP-SE algorithm [5] estimates the *S*, *W*, and *P* parameters from this spectrum. Figure 3 shows the variation in the *S* parameter in Cd-

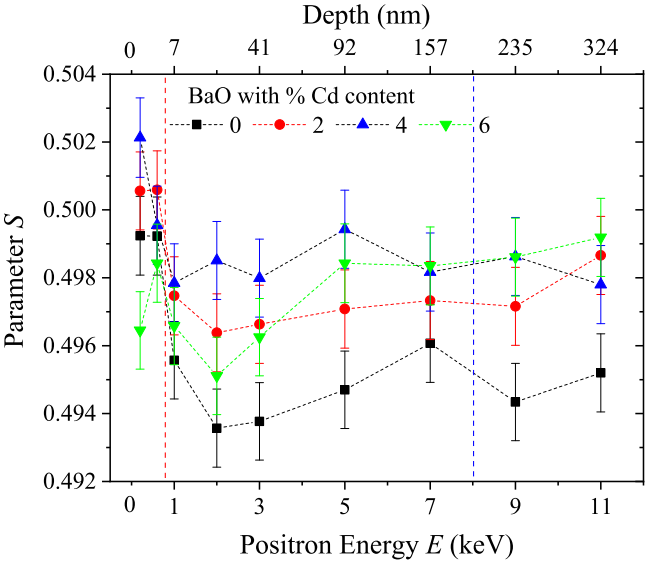

Figure 3. *S* parameter versus positron energy *E* (keV) and depth *z* (nm) for the Cd-doped BaO samples (0, 2, 4, and 6% Cd-doped).

doped BaO due to altering the positron implantation energy from 0.2 keV to 11 keV. The average depth at which positrons are implanted into the sample is estimated from [11,12,22]

$$z(E) = (40/\rho)E^{1.6} \tag{2}$$

where $z(E)$ is the average depth in nm, ρ is the sample density in g/cm^3 and E is the incident positron energy in keV.

With a BaO density of 5.72 g/cm^3, the average depth of positron penetration is displayed on the top horizontal axis in Figure 3, corresponding to the positron energy at the bottom axis. In the case of low positron implantation energy, specifically below 1 keV (with a penetration depth of up to 6 nm), the accumulation and reflection of electrons lead to surface-related phenomena. As a result, the discussion in this context excludes the immediate surface region, which is indicated by a vertical red line in Figure 3. The film thickness of each sample falls within the range of 150–200 nm. To obtain information about the interface between the film and the substrate, as indicated by the vertical blue line in Figure 3, the average positron energy should be approximately 8 keV, as determined by Equation (2). Hence, we are particularly interested in energies ranging from 1 to 8 keV, which correspond to film thicknesses ranging from approximately 6 to 200 nm, respectively. We obtain this information mostly from the glass substrate at energies above 8 keV (higher than 200 nm).

The average S parameter is 0.4947 for neat BaO in the film region from 6 to 200 nm. Adding 2, 4, and 6% Cd to BaO results in average increases in the S parameter to 0.4970, 0.4984, and a subsequent reduction to 0.4969, respectively. These values are somewhat lower than the Si reference value. The link with the AFM observations indicates that when Cd doping increases, the crystallite sizes decrease, leading to an increase in the size and quantity of vacancy defects on the surface of the crystallites and the interstitial voids among them (especially triple points). As the particle size decreases, the number of vacancy defects on the surface of crystallites increases, and the number of interstitial void defects decreases. We note a comparable influence on the rising S parameter as an indicator of vacancy defects as a competition of surface and interstitial defects. The crystallite size of BaO doped with 6% Cd markedly decreases to 1.4 nm, leading to a decrease in vacancy disorder attributed to diminished interstitials, which in turn results in a decreased S parameter. On the other hand, the energy band gap increases with increasing Cd content, as shown in Table 1. Similarly, we observed an increase in the S parameter with increasing Cd content, with the exception of 6%, which again led to a decrease in interstitial defects. In materials characterised by a larger band gap, such as insulators and semiconductors, positrons tend to preferentially annihilate with valence electrons or become trapped at defects, resulting in increased variations in the S parameter. The S parameter and the energy band gap measure independent material properties, although their dependence on the electronic structure is linked. DBS shows localised electronic structures, whereas the band gap shows a material's electronic structure. Analysing defect behaviour, electrical characteristics, and material functionality requires relating each to the others.

Besides, the P parameter, which quantifies the porous structure depicted in Figure 4, remains relatively horizontal in the film. Doping BaO with Cd results in a decrease in P as

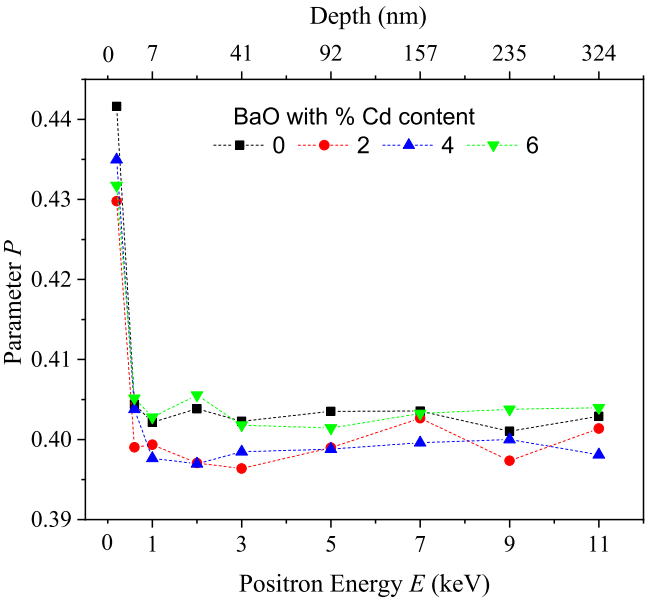

Figure 4. *P* parameter versus positron energy *E* (keV) and depth *z*(nm) for the Cd-doped BaO samples (0, 2, 4, and 6% doped with Cd).

the percentage of substitution increases. As predicted by the *P* parameter, the porosity decreases with increasing Cd concentration since the voids in the pores of the crystallites decrease. However, at a substitution percentage of 6%, *P* returns to nearly its original value, which can be attributed to the decrease in interstitial voids when the crystallites are radically reduced to 1.4 nm. In other words, it has a nearly inverse relationship with the *S* parameter [12,13].

Figure 5 plots the W parameter against the S parameter for the Cd-doped BaO samples, displaying the error-weighted linear regression along with its respective data colour for each set of data. The black square represents the pure sample of BaO. The data for each Cd-doped sample shifted to the right with increasing S parameter. The red and round symbols represent 2% Cd, the blue and upper triangles represent 4% Cd, and the green and lower triangles represent 6% Cd. The data are shown with S and W error bars, indicating that the scattered data are near each line. The figure indicates that the undoped and Cd-doped BaO films exhibit distinct lines, indicating the presence of different types of vacancy defects. Spreading along the line refers to the phenomenon in which the depth of vacancy defects inside the film changes. Figure 3 illustrates this phenomenon. With Cd doping, the S parameter and vacancy defects from Cd substitution increase, whereas the W parameter changes within the error bars, except for the 4% Cd sample, for which the W parameter decreases.

3.6. Positron annihilation lifetime spectroscopy (PALS) results

The samples analysed in this study consisted of BaO films doped with Cd and deposited onto a glass substrate. The film has a thickness of approximately 150–200 nm. To

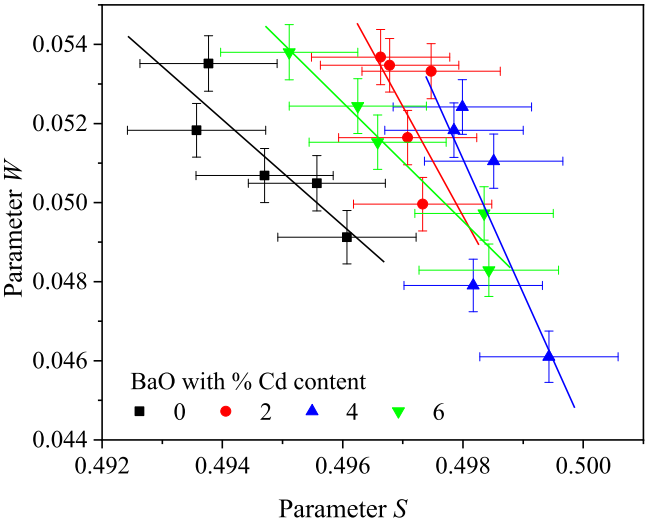

Figure 5. The *W* parameter is plotted versus the *S* parameter with the error-weighted best fit line.

conduct PALS spectroscopy on this film, the film thickness must be approximately one-fifth mm, as this thickness falls within the range of the highest energy positron penetration depth. However, it is still possible to obtain information regarding the defects in the film by utilising the PALS approach. To achieve this objective, two samples must be included in the positron source. One of the samples utilises a glass substrate, whereas the other sample consists of a film layered on top of the substrate. Thus, we have mostly obtained information from the glass substrate. Initially, we started working with glasses to obtain lifetime data. We subsequently substituted one of the samples with the film. We utilised the LT9.3 programme [15,23] to convolute the data of all the samples with the three lifetimes and intensities. The measured values for the lifetimes (τ_2 and τ_3) and intensities (I_2 and I_3) are listed in Table 2. The value of τ_1 is set at 0.125 ns, which corresponds to the p-Ps state and remains relatively constant in both vacuum and matter.

The lifetime of o-Ps is correlated with the presence of large voids in the glass and agrees with the values reported in the literature [24]. The parameters of direct annihilation, namely, τ_2 and I_2, account for slightly more than 60% of the dominating annihilation processes. These processes are associated with vacancy spaces that are not sufficiently large to form o-Ps. To examine the impact of the BaO film on the lifetime

Table 2. PALS parameters of lifetimes (τ_2 and τ_3) and intensities (I_2 and I_3) in terms of the Cr content (x concentration), where the intensities are normalised to $I_1 + I_2 + I_3 = 1$ and τ_1 is fixed to 0.125 ns.

Samples	x	τ_2 (ns) (±0.001)	I_2(%) (±0.3)	τ_3 (ns) (±0.005)	I_3(%) (±0.2)
Glass substrate		0.367	62.8	0.961	21.5
Glass + BaO	0	0.366	60.5	0.948	24.1
Glass + %2 Cd-BaO	0.02	0.348	62.7	0.917	24.4
Glass + %4 Cd-BaO	0.04	0.356	63.7	0.930	23.5
Glass + %6 Cd-BaO	0.06	0.341	61.5	0.902	25.7

parameters, we conducted the following procedure. Initially, we obtained literature values for the two lifetime fits of BaO, which were recorded as 0.203 ns with intensities of 78.7% and 0.406 ns with the remaining values [25]. Owing to the limited thickness of our sample, which consists of very thin films on a glass substrate, we had difficulty accurately assessing similar lifetime values. However, the BaO films present in our samples may contribute to the direct annihilation parts, namely, τ_2 and I_2, of the PALS. This is because BaO has a similar contribution of approximately 0.406 ns, as reported in the literature. Thus, in Figure 6, we have plotted the relationship between I_2 and the Cd contents on the right vertical axis and the average S parameters on the left axis. The I_2 value tended to increase as the Cd concentration increased, reaching its peak at 4% Cd, after which it decreased. Similar behaviour can be observed for the $< S >$ parameter, which serves as a metric for vacancy defects in a sample.

With respect to the defect types in BaO, several unique vacancies are expected, such as single Ba vacancy (V_{Ba}), single O vacancy (V_O), divacancy (V_{Ba}-V_O) and their clusters $(V_{Ba}\text{-}V_O)_n$, as well as vacancy-antisite pairs ((V_{Ba}-Ba_O) and (V_O-O_{Si})), which can be filled with impurities or doped atoms.

The charge state of an oxygen defect in BaO depends on the specific type of defect and its environmental conditions. The primary types of oxygen defects in BaO are oxygen vacancies (V_O) and oxygen interstitials (O_i), whose charge states vary on the basis of factors such as the Fermi level position, chemical potential, temperature, and doping conditions [26,27]. Oxygen interstitials are rare and typically function as acceptors. The charge states of the oxygen vacancies may be anticipated as neutral V_O^0, singly positively charged V_O^+, or doubly positively charged V_O^{2+}. For comparison, oxygen vacancies in ZnO are typically regarded as donors that facilitate the n-type conductivity observed in semiconductor materials [26,27]. Under n-type circumstances, the defect charge state is contingent upon the position of the Fermi level, generally manifesting as V_O^+ and V_O^{2+}. Consequently, positron trapping is less efficient in V_O^+ and V_O^{2+} because of the repulsive interaction between the positively charged vacancy and the positron, with the exception of neutral V_O^0 defects. Conversely, BaO often functions as an insulator and possesses a

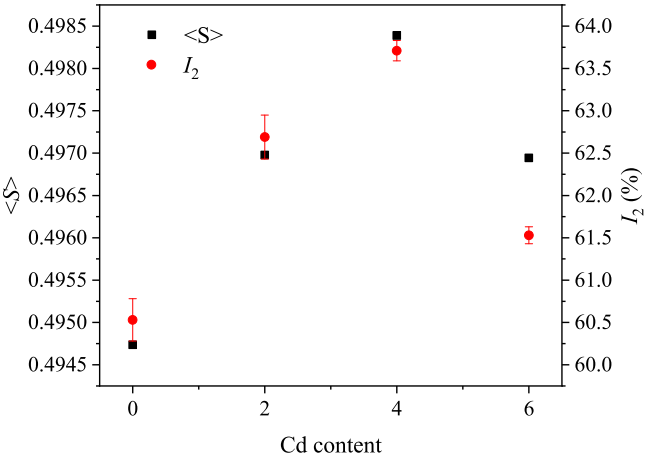

Figure 6. Average S parameter $< S >$ and intensity I_2 versus the Cd content.

structure akin to that of rock salt. The electronic band structure significantly differs from that of ZnO. The charge states of the oxygen vacancies in BaO are typically V_O^0 or V_O^+, although the high dielectric constant of BaO may alter their characteristics in comparison to those of ZnO. The oxygen vacancies in BaO are often less positively charged, perhaps facilitating the trapping of positrons due to its dielectric characteristics. Consequently, in a pure sample, the occurrence of oxygen defects, such as V_O^0 or V_O^+, is anticipated to be detected mostly in the DBS and PALS data.

Doping Cd into BaO is anticipated to substitute Ba without causing charge imbalance, as both Cd^{2+} and Ba^{2+} possess identical charges. Moreover, the introduction of Cd replacement results in the formation of Ba vacancy defects. Under oxygen-rich circumstances with low Cd doping, Cd may create Ba vacancies to maintain charge balance. This indicates an elevation in the S parameter in the DBS and I_2 in the PALS analysis. This also appears as a significant shift in the S parameter axis in the W–S graph depicted in Figure 5. Furthermore, Cd^{2+} (95 pm) is smaller than Ba^{2+} (135 pm), resulting in local lattice contraction [28]. This results in a decrease in the lifetime τ_2 in the PALS measurements. With the addition of 4% Cd, the W–S plot in Figure 5 still shows an increase in the S parameter but a decrease in the W parameter; this increase suggests that more vacancy defects are produced, whereas the decrease indicates that Cd reduces the Doppler shift as a chemical effect, resulting in positron annihilation at the inner electron with a reduced Doppler effect. Doping in an oxygen-deficient environment with a 6% Cd concentration may result in the formation of extra oxygen vacancies to preserve charge neutrality. If extra cadmium is supplied beyond substitutional limits, cadmium atoms may occupy barium vacancy sites or interstitial sites. A reduction in Ba vacancies leads to a transition to O defects in the W–S plot depicted in Figure 5. Consequently, the S and I_2 values decreased at the 6% Cd concentration.

The correlation between Cd doping and the DBS and PALS parameters provides substantial insights into the material features of defect behaviour. This improves our understanding of how doping can precisely alter defect characteristics, potentially facilitating applications across diverse technological domains. Establishing these links enhances material performance through tailored doping procedures, thereby improving future research and applications.

4. Conclusion

Pure and Cd-doped BaO films were investigated via AFM, UV–Vis, PALS, and DBS techniques. The AFM analysis indicated that adding Cd reduced the size of the crystallites from 150 nm to 1.4 nm and improved the surface quality. The transmittance analysis via UV–Vis spectroscopy revealed that the amount of light passing through pure BaO decreased from 70% to 50% when Cd was added. The energy bandgap changed from 3.467 to 3.728 eV. The results obtained from this experimental part showed that the the synthesised samples are of good qualities and can be used in optoelectronic applications (solar photocells) or gas detection (gas sensors)

The DBS measurements revealed that the S parameter, a measure of vacancy defects, increased with increasing Cd doping. Correlations emerged between increased surface area, size reduction, and interstitial voids. PALS work has been carried out with glass information but still has some information extracted for BaO contribution to the

vacancy. We had similar behaviour for the I_2 value and the < S > parameter, as depicted in Figure 6. Therefore, defect analysis in BaO reveals that the primary defects are neutral or less positively charged oxygen vacancies to be detected by the DBS and PALS techniques. The introduction of Cd in BaO causes Ba vacancies to maintain charge. The impact of these defects is reflected in a notable increase in the S and I_2 parameters. This can also be pictured in the S–W graph.

The intricate relationship between Cd doping and material defect behaviour has significant implications for practical applications. As demonstrated by the data in Figure 6, a 6% concentration of Cd leads to a notable decrease in the S and I_2 values, suggesting that optimal doping levels can effectively modify the characteristics of defects within the material. The correlation between Cd doping and parameters such as DBS and PALS not only illuminates the underlying mechanisms of defect behaviour but also highlights the possibility of tailoring material properties through precise doping techniques. By deepening our grasp of how doping influences defects, we pave the way for enhanced material performance and open new avenues for future research endeavours aimed at optimising these materials for various technological applications.

Disclosure statement

No potential conflict of interest was reported by the author(s).

References

[1] S. Alarifi, D. Ali, and W. Al-Bishri, Multimodal iron oxide (Fe_3O_4)-saturated lactoferrin nanocapsules as nanotheranostics for real-time imaging and breast cancer therapy of claudin-low, triple-negative ($ER^-/PR^-/HER2^-$). Nanomedicine 11 (2016), pp. 249.
[2] A.Z. Bazeera and M.I. Amrin, Synthesis and characterization of barium oxide nanoparticles. IOSR J. Appl. Phys. 01 (2017), pp. 76.
[3] N. Moradbeigi, A. Bahari, and S. Ghasemi, Effect of molybdenum doping on the catalytic activity of VS_2/CNT for the oxygen reduction reaction in alkaline media. New J Chem 47 (2023), pp. 1291.
[4] A. Sümer, Effects of composition on catalytic activities of molybdenum doped platinum nanoparticles. Turk. J. Chem. 44 (2020), pp. 1016.
[5] E. Sundharam, A.K.S. Jeevaraj, and C. Chinnusamy, Effect of ultrasonication on the synthesis of barium oxide nanoparticles. J. Bionanoscience 11 (2017), pp. 310.
[6] Y. Cui, J. Chen, Y. Zhang, X. Zhang, W. Lei, Y. Di, and Z. Zhang, Enhanced performance of thermal-assisted electron field emission based on barium oxide nanowire. Appl. Surf. Sci. 396 (2017), pp. 1108.
[7] A.O. Mousa, N.A. Nema, and H.H. Hasan, Effect of annealing on barium oxide (BaO) thin films prepared by chemical spray pyrolysis (CSP) technique. J. Chem. Pharm. Res. 8(8) (2016), pp. 832.
[8] P.N. Nirmala and G. Suresh, Synthesis of barium oxide nanorod by chemical bath deposition. Turk. J. Phys. 36(3) (2012), pp. 392–397.
[9] S.P. Prabhavathi, J. Punitha, P.S. Rajam, R. Ranjith, G. Suresh, N. Mala, and D. Maruthamuthu, Simple methods of synthesis of copper oxide, zinc oxide, lead oxide and barium oxide nanoparticles. J. Chem. Pharm. Res. 6(3) (2014), pp. 1472.
[10] F.S. Razavi, M. Hajizadeh-Oghaz, O. Amiri, M.S. Morassaei, and M. Salavati-Niasari, Barium cobaltite nanoparticles: Sol-gel synthesis and characterization and their electrochemical hydrogen storage properties. Int. J. Hydrog. Energy 46 (2021), pp. 886.

[11] Y.C. Jean, P.E. Mallon, and D.M. Schrader, *Principles and Applications of Positron and Positronium Chemistry*, World Scientific Publishing, Singapore, 2003 doi: 10.1142/5086.
[12] M. Izerrouken, R. Hazem, U. Yahsi, S.E. Naceri, C. Tav, S. Küzeci, A. Sari, F. Haid, A. Ishaq, O. Menchi, and M. Ghamnia, Heavy ion irradiation induced defects in Zircaloy-4. Phys Scr 96 (2021), pp. 045008 doi: 10.1088/1402-4896/abe3bf.
[13] M. Izerrouken, R. Hazem, S. Kuzeci, C. Tav, U. Yahsi, and S. Limam, Electronic ionisation-induced annealing of pre-existing defects in Al_2O_3 and CaF_2 single crystals. Philos. Mag. 102 (2022), pp. 283.
[14] S. Awad, A. Al-Rashdi, E.E. Abdel-Hady, Y.C. Jean, and J.D. Van Horn, Free volume properties of the zinc oxide nanoparticles/waterborne polyurethane coating system studied by a slow positron beam. J. Compos. Mater. 53 (2019), pp. 1765.
[15] J. Kansy, Microcomputer program for analysis of positron annihilation lifetime spectra. Nucl. Instrum. Methods Phys. Res. Section A: Accel. Spectrom. Detect. Assoc. Equip. 374 (1996), pp. 235.
[16] I. Horcas, R. Fernández, J.M. Gómez-Rodríguez, J. Colchero, J. Gómez-Herrero, and A.M. Baro, WSXM: A software for scanning probe microscopy and a tool for nanotechnology: A software for scanning probe microscopy and a tool for nanotechnology. Rev. Sci. Instrum. 78 (2007), pp. 013705 doi: 10.1063/1.2432410.
[17] M.A. Dahamni, M. Ghamnia, S.E. Naceri, C. Fauquet, D. Tonneau, J.-J. Pireaux, and A. Bouadi, Spray pyrolysis synthesis of pure and MG-doped manganese oxide thin films. Coatings 11 (2021), pp. 598 doi: 10.3390/coatings11050598.
[18] A. Ouhaibi, M. Ghamnia, M.A. Dahamni, V. Heresanu, C. Fauquet, and D. Tonneau, The effect of strontium doping on structural and morphological properties of ZnO nanofilms synthesized by ultrasonic spray pyrolysis method. J. Sci: Adv. Mater. Devices 3 (2018), pp. 29.
[19] J. Tauc, *Amorphous and Liquid Semiconductors*, Plenum Publishing Company Ltd, London, 1974 doi: 10.1007/978-1-4615-8705-7.
[20] N. Jahan and M.A. Ansari, Structural and optical properties of BaO nanoparticles synthesized by facile Co-precipitation method. Mater. Highlights 2(1-2) (2021), pp. 23–28 doi: 10.2991/mathi.k.210226.001.
[21] F. Naz and K. Saeed, Synthesis of barium oxide nanoparticles and its novel application as a catalyst for the photodegradation of malachite green dye. Appl. Water Sci. 12 (2022), p. 121 doi: 10.1007/s13201-022-01649-9.
[22] A. Arrar, M. Benhaliliba, A. Boukhachem, U. Yahşi, C. Tav, A. Yumak, and M. Amlouk, Optical and photoluminescence spectroscopy analysis and Doppler broadening annihilation radiation studies of perovskites based on La1-XNiXMnO2.75 thin layers. Optik 224 (2020), p. 165678 doi: 10.1016/j.ijleo.2020.165678.
[23] Y.C. Jean, P.E. Mallon, and D.M. Schrader, *Principles and Applications of Positron and Positronium Chemistry*, World Scientific Publishing, Singapore, 2003 doi: 10.1142/5086.
[24] Y. Sasaki, Y. Nagai, H. Ohkubo, K. Inoue, Z. Tang, and M. Hasegawa, Positronium in silica-based glasses. Radiat. Phys. Chem. 68 (2003), pp. 569.
[25] V.T. Adonkin, B.M. Gorelov, D.V. Morozovskay, and V.M. Ogenko, Effect of water-adsorption on positron-annihilation lifetimes in barium oxide and barium peroxide. Colloid Surf. A 101 (1995), pp. 233 doi: 10.1016/0927-7757(95)03181-C.
[26] L. Liu, Z. Mei, A. Tang, A. Azarov, A. Kuznetsov, Q.-K. Xue, and X. Du, Oxygen vacancies: The origin of n-type conductivity in ZnO. Phys. Rev. B 93 (2016), p. 235305 doi: 10.1103/PhysRevB.93.235305.
[27] A. Janotti and C.G. Van de Walle, Native point defects in ZnO. Phys. Rev. B 76 (2007), p. 165202 doi: 10.1103/PhysRevB.76.165202.
[28] R.D. Shannon, Revised effective ionic radii and systematic studies of interatomic distances in halides and chalcogenides. Acta Crystallogr. Sect. A 32 (1976), pp. 751 doi: 10.1107/s0567739476001551.